ACADEMIC PRESS

Available online at www.sciencedirect.com
SCIENCE DIRECT®

NeuroImage

NeuroImage 19 (2003) 1329–1336

www.elsevier.com/locate/ynimg

Properties of MEG tomographic maps obtained with spatial filtering

J. Gross,[a,*] L. Timmermann,[a] J. Kujala,[b] R. Salmelin,[b] and A. Schnitzler[a]

[a] *Department of Neurology, Heinrich-Heine-University, D-40225 Duesseldorf, Germany*
[b] *Brain Research Unit, Low Temperature Laboratory, Helsinki University of Technology, FIN-02015, HUT, Espoo, Finland*

Received 26 September 2002; accepted 3 February 2003

Abstract

Magnetoencephalography (MEG) has, in comparison with other functional imaging modalities, unique properties which makes it the prime candidate for the noninvasive investigation of long-range oscillatory interactions in the human brain. Recent methodological developments based on spatial filtering introduced the computation of functional tomographic maps covering the entire brain and representing the distribution of coherence to a given reference signal or the distribution of power. Because of the spatially inhomogeneous sensitivity profile of the MEG sensors, the spatial resolution of the resulting functional maps is not isotropic across the brain. Here, we introduce a convenient analytic expression for the computation of the spatial resolution at any given point in the brain. We derive the dependence of the resolution on the signal-to-noise ratio and on the changes of the leadfields. The resolution map can be displayed on anatomical MRI in the same way as the functional maps. In addition, we establish a procedure for computing a confidence volume of local maxima which is based on a bootstrap method. The confidence volume is a measure for the uncertainty of the localization. It is important for assigning local maxima of activation to specific anatomical structures and may be used to test for differences in localization between different experimental conditions.

Keywords: Spatial filter; Beamformer; Resolution; Confidence volume; Tomographic map; DICS

Introduction

Although most functional imaging studies are still designed to statically assign brain function to brain structure, it is increasingly recognized that human brain function can only be adequately studied by taking into account the highly dynamic and transient nature of activity patterns and interactions evolving simultaneously in space and time. Magnetoencephalography (MEG) and electroencephalography (EEG) provide the appropriate temporal resolution to study the dynamics of brain processes. Additionally, state-of-the-art MEG/EEG systems offer a dense spatial sampling of the whole scalp with a variety of sensors.

Recent methodological developments further increased the potential of MEG/EEG to study brain dynamics. These methodological advances are taking place mainly in the areas of, first, time series analysis (MEG/EEG) and, second, tomographic mapping of oscillatory activity and coupling (MEG). In the first area, substantial progress has been made in the characterization of strength and direction of phase synchronization of two oscillatory signals (Varela et al., 2001; Rodriguez et al., 1999; Lachaux et al., 1999; Tass et al., 1998; Rosenblum and Kurths, 1998; Rosenblum and Pikovsky, 2001).

In the second area, the main development is the transition from sensor-based measures to source-based mapping of oscillatory activity (Gross et al., 2002, 2001; Jensen and Vanni, 2002; Brovelli et al., 2002; Singh et al., 2002; Taniguchi et al., 2000) and coupling (Gross et al., 2002, 2001). In contrast to the classical model of pointlike sources (multidipole model) we use tomographic maps of oscillatory power or coherence. These raw functional maps can be subjected to further statistical analysis. The tomographic maps can be spatially normalized into a common anatomical frame and may be displayed similar to results of fMRI or PET studies.

* Corresponding author. Department of Neurology, Heinrich-Heine-University Duesseldorf, Moorenstrasse 5, D-40225 Duesseldorf, Germany. Fax: +49-0-211-811-9033.

E-mail address: jgross@uni-duesseldorf.de (J. Gross).

1053-8119/03/$ – see front matter
doi:10.1016/S1053-8119(03)00101-0

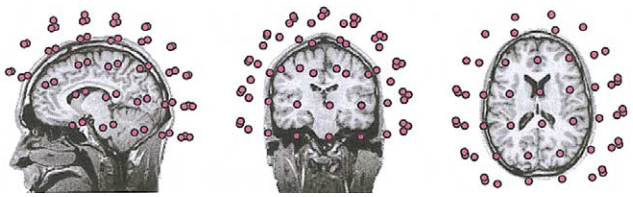

Fig. 1. Sensor position. The sensor positions of the Neuromag-122 system are shown as colored dots with respect to the subjects anatomical magnetic resonance image.

In this paper, we present a new technique for evaluating the spatial resolution of tomographic maps obtained by spatial filtering (van Veen et al., 1997; Gross et al., 2001; Sekihara and Scholz, 1996; Robinson and Vrba, 1997). A proper characterization of these tomographic maps is of high interest and relevance because they have a nonuniform spatial resolution depending on the data and on the location in the brain. An efficient and reliable assessment of the maps' properties is important for their statistical evaluation and scientific interpretation.

The original work presented here is related to the concept of the point spread function (PSF) and the resolution matrix (de Peralta-Menendez et al., 1997; Babiloni et al., 2001; Liu et al., 2002; Lutkenhoner and de Peralta-Menendez, 1997; Dale et al., 2000). In contrast to the numerical computations performed in the previous work, we use an analytic estimate of the resolution of tomographic maps and a bootstrap approach for the computation of a confidence volume for the location of local maxima.

The topology of data space

The coordinate system used in this paper is defined in the following way. A line connecting the left and right periauricular points defines the x axis. The y axis is perpendicular to the x axis and points to the nasion. The z axis is the normal vector to the plane spanned by the x and y axis.

All computations were performed using the sensor configuration of the Neuromag-122 system (Ahonen et al., 1993). The positions of the 122 planar gradiometers with respect to the subjects head were taken from a real experiment (see Fig. 1).

Let us first define the source space Q as the space of all possible current density distributions $\mathbf{J}$ in the human brain. For the sake of clarity the time-dependence of $\mathbf{J}$ is not explicitly noted in the following equations. We further define the data space D as the space of all possible measurements $\mathbf{m}$. Using an MEG system with N sensors results in D being a subspace of R^N. Performing a measurement corresponds to the application of an operator $\mathcal{L}$ to $\mathbf{J}$ which leads to the measured data $\mathbf{m}$

$$\mathbf{m} = \mathcal{L}\mathbf{J}. \tag{1}$$

$\mathcal{L}$ is the Leadfield operator which is defined as

$$\mathcal{L}\mathbf{J}(\mathbf{r}') = \int_G \mathbf{L}(\mathbf{r},\mathbf{r}')\mathbf{J}(\mathbf{r}')d^3r', \tag{2}$$

where the integration is performed over the entire brain G. $\mathbf{L}(\mathbf{r},\mathbf{r}')$ is the leadfield

$$\mathbf{L}_i(\mathbf{r}',\mathbf{r}_0) = \sum_j \omega_j \int_{F_j} \mathbf{B}(\mathbf{r}_j',\mathbf{r}_0,\mathbf{e}_i) \cdot \mathbf{n}_j d^2r_j'. \tag{3}$$

In Eq. (3) $\mathbf{B}(\mathbf{r}_j',\mathbf{r}_0,\mathbf{e}_i)$ is the magnetic field at $\mathbf{r}_j'$ due to a dipolar source at $\mathbf{r}_0$ with orientation $\mathbf{e}_i$. $\mathbf{e}_i$ is a unit vector in

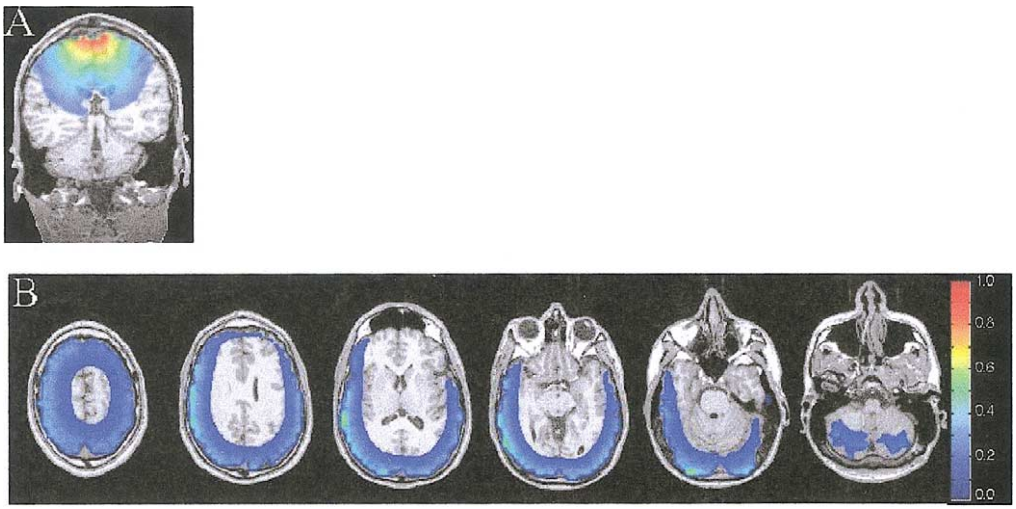

Fig. 2. Leadfield of a sensor. (A) The absolute value of the leadfield of a single sensor is shown overlayed on a coronal MRI slice. (B) The sum of the absolute values of the leadfields of all sensors is color-coded at each point in six axial slices of an anatomical MR image. The head position relative to the sensors was taken from a real experiment.

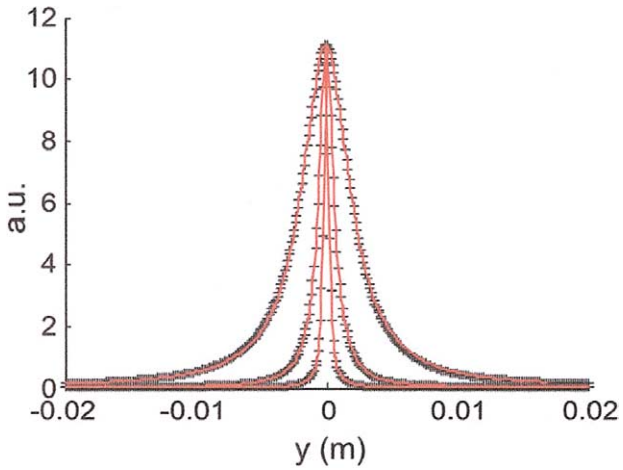

Fig. 3. Lorentzian profile of a power peak. The power estimate of the LCMV filter is plotted along the y axis (marked with +) for three different SNR (10, 20, and 30 dB). The source is at $y = 0$. The red line represents the Lorentzian profile fitted to the power values.

direction x, y, z of the Cartesian coordinate system. j is the index of the MEG coils and ω_j is the winding direction of coil j. Integration is performed over the coil surface F_j with the corresponding normal vector $\mathbf{n}_j$.

The solution of the forward problem for a given current density distribution **J** can then be written as

$$\mathbf{m}(\mathbf{r}) = \int_G \mathbf{L}(\mathbf{r},\mathbf{r}')\mathbf{J}(\mathbf{r}')d^3r' \ , \tag{4}$$

The leadfield describes the sensitivity of the MEG system to a source with a given orientation at a given point in the brain.

The properties of the leadfields determine the topology of data space. A proper characterization of this topology is important for the interpretation of results and has to be taken into account for statistical assessment of significances. Well-known features of MEG recordings are the insensitivity to radial sources and a decreased sensitivity with increasing distance from the sensors. These features can be directly related to properties of the leadfield. If a current density distribution consists only of radial sources, the integration in Eq (4) yields zero for a spherical volume conductor model because there is no overlap between $\mathbf{L}(\mathbf{r},\mathbf{r}')$ and **J**. The sensitivity of a single sensor is displayed in Fig. 2A. The decrease of sensitivity with increasing distance from the sensor can be clearly seen.

Fig. 2B shows the sum of the norm of the leadfields of all sensors, on six axial slices. The color thus corresponds to the overall magnitude of a response that a point source with unit strength elicits in the sensor array and represents a measure of sensitivity to a given anatomical area. The figure underlines the well-known fact that the sensitivity decreases

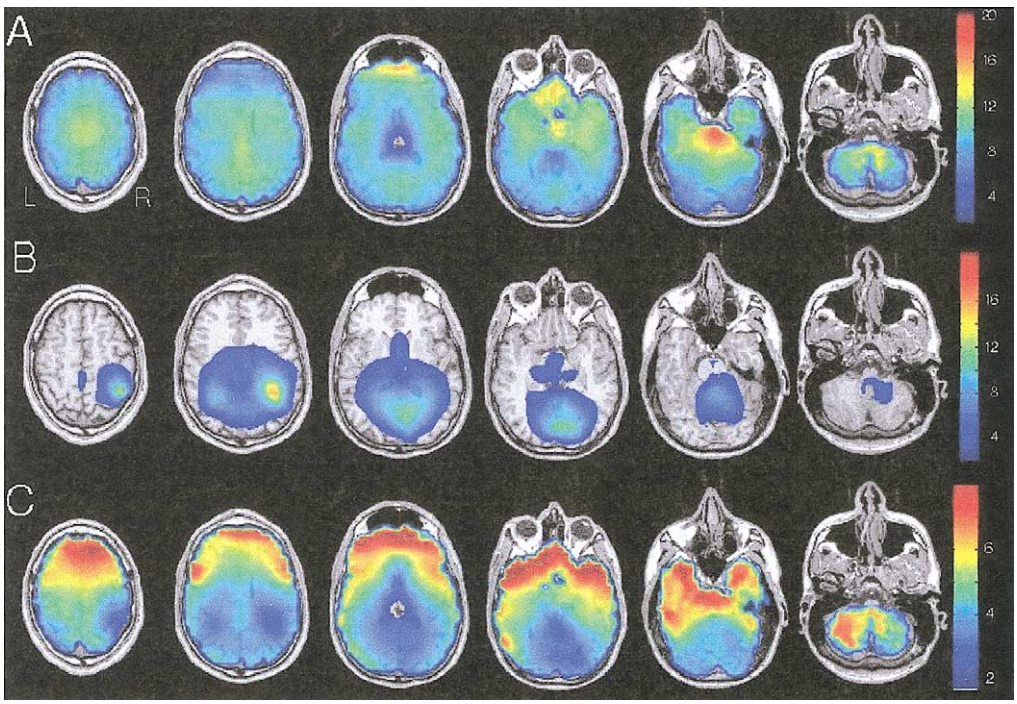

Fig. 4. Map of FWHM. (A) The FWHM (in mm) at SNR 20 dB is color-coded and overlaid on axial anatomical MRI slices. (B) The ratio of power to noise is color-coded and overlaid on axial anatomical MRI slices. (C) The FWHM (in mm) at SNR 20 dB is color-coded and overlaid on axial anatomical MRI slices. Now the power at each voxel is taken into account. Colors were clipped to a maximum of 8 mm to reveal more relevant details. L, R mark the left and right hemisphere, respectively.

with the distance to the sensors. Sensors are most sensitive to cortical areas.

The spatial profile of DICS

We have recently developed a technique, DICS (dynamic imaging of coherent sources), for the tomographic mapping of power and coherence in the entire brain (Gross et al., 2001). DICS uses a linear transformation which belongs to the general category of linearly constrained minimum variance (LCMV) beamformer (van Veen et al., 1997). The results presented here can be directly applied to all LCMV beamformers in the time or frequency domain. The transformation is obtained by minimizing the variance of the spatial filter output with the constraint that the activity in a specific frequency band of the source at position $\mathbf{r}$ passes with unit gain. The mathematical formulation is

$$\min[\mathscr{E}\{|\mathbf{AD}|^2\} + \alpha|\mathbf{A}|^2] \text{ subject to } \mathbf{AL}(\mathbf{r}) = \mathbf{I}, \quad (5)$$

where $\mathscr{E}\{\cdot\}$ denotes the expectation value and the matrix $\mathbf{D}$ contains the Fourier transformed data. $\mathbf{I}$ is the unit matrix and α is the regularization parameter. The solution is

$$\mathbf{A}(\mathbf{r}, f) = (\mathbf{L}^T(\mathbf{r})\mathbf{C}_r(f)^{-1}\mathbf{L}(\mathbf{r}))^{-1}\mathbf{L}^T(\mathbf{r})\mathbf{C}_r(f)^{-1}, \quad (6)$$

with $\mathbf{C}_r(f) = \mathbf{C}(f) + \alpha\mathbf{I}$, where $\mathbf{C}(f)$ is the cross spectral density matrix at frequency f or averaged across a frequency band centered at f, and superscript T indicates the matrix transpose. The variance of the estimated activity at a given point $\mathbf{r}$ is $(\mathbf{AD})(\mathbf{AD})^T$ which leads to the following simple expression for the power P

$$P(\mathbf{r}, f) = [\mathbf{L}^T(\mathbf{r})\mathbf{C}_r(f)^{-1}\mathbf{L}(\mathbf{r})]^{-1}. \quad (7)$$

This expression can be employed for all points of a regular 3D grid covering the entire brain leading to a tomographic map of power at frequency f.

We will now show that we can write Eq (7) in a form that allows the simple extraction of the full width at half maximum (FWHM) of the point spread function (PSF). This is achieved by, first, decomposing $\mathbf{C}$ into separate matrices for the signal and the noise space and, second, by a polynomial expansion of the spatial change of leadfields.

It is evident from Eq. (7) that the properties of the tomographic map depend on the leadfields and on $\mathbf{C}$ (and thus on the data). The symmetric matrix $\mathbf{C}$ can be decomposed by singular value decomposition

$$\mathbf{C} = \mathbf{USU}^T \quad (8)$$

where $\mathbf{S}$ is a diagonal matrix of eigenvalues and $\mathbf{U}$ contains orthogonal vectors. The inverse of $\mathbf{C}$ can be written as

$$\mathbf{C}^{-1} = \mathbf{US}^{-1}\mathbf{U}^T = \sum_{i=1}^{N}\mathbf{S}_{i,i}^{-1}\mathbf{U}_i^T\mathbf{U}_i = \mathbf{S}_{1,1}^{-1}\mathbf{U}_1^T\mathbf{U}_1 + \mathbf{S}_{2,2}^{-1}\mathbf{U}_2^T\mathbf{U}_2 + \cdots. \quad (9)$$

The last term represents a sum of weighted orthogonal projection matrices. True source locations correspond to projections with large eigenvalues. If $\mathbf{r}$ corresponds to the position of the only source and we insert the expansion of $\mathbf{C}$ in Eq (7) we obtain

$$P(\mathbf{r}, f) = [\mathbf{S}_{1,1}^{-1}\mathbf{L}^T(\mathbf{r})\mathbf{U}_1{}^T\mathbf{U}_1\mathbf{L}(\mathbf{r}) + \mathbf{S}_{2,2}^{-1}\mathbf{L}(\mathbf{r})^T(\mathbf{I} - \mathbf{U}_1{}^T\mathbf{U}_1)\mathbf{L}(\mathbf{r})]^{-1}. \quad (10)$$

Again, $\mathbf{U}_1^T\mathbf{U}_1$ in the first addend is a projection matrix on the vector $\mathbf{U}_1$ (which represents the source) and $(\mathbf{I} - \mathbf{U}_1^T\mathbf{U}_1)$ in the second addend is the complement space. Here, we use $\mathbf{S}_{2,2}^{-1}$ in the second addend due to the fact that the noise space has a flat eigenvalue spectrum.[1]

A closer examination of Eq. (10) reveals valuable information about the resolution and structure of power maps. At the true source location, $\mathbf{L}$ is in the space described by the projection matrix $\mathbf{U}_1^T\mathbf{U}_1$. The second addend is zero because there is (in the ideal case) no component of $\mathbf{L}$ in the complement space of $\mathbf{U}_1^T\mathbf{U}_1$. By moving away from the source, $\mathbf{L}$ has more components in noise space which are suppressed due to the small eigenvalues. Consequently, we expect a peak at the true source location and a decrease in power with increasing distance to the true source. The rate of decrease depends on the signal-to-noise (SNR) ratio (which is reflected in the eigenvalues in S) and the spatial change of $\mathbf{L}$. The higher the SNR, the larger is the separation between signal and noise eigenvalues which leads to a more focal representation of the source in the power map. Similarly we get a more focal representation of the source if the leadfields show a large change while moving away from the source. The sharpness of the representation of a point source (the point spread function PSF) can be quantified with the full width at half maximum (FWHM) of the peak. The FWHM is related to the ability to separate two activations.

From Eq. (10) we can derive a simple expression for this dependence of P on the change in leadfields and the SNR of the data

$$P(\mathbf{r},f) = [\mathbf{S}_{1,1}^{-1}\mathbf{L}^T(\mathbf{r}_0)\mathbf{L}(\mathbf{r}) + \mathbf{S}_{2,2}^{-1}(\mathbf{I} - \mathbf{L}^T(\mathbf{r}_0)\mathbf{L}(\mathbf{r}))]^{-1}, \quad (11)$$

where $\mathbf{r}_0$ corresponds to the true source location. We obtain the following expression

$$P = \frac{S_{1,1}}{R_L(\mathbf{r}_0,\mathbf{r}) + \frac{S_{1,1}}{S_{2,2}}(1 - R_L(\mathbf{r}_0,\mathbf{r}))}, \quad (12)$$

[1] Equation (10) can be easily modified for the case of M sources.

where $R_L(\mathbf{r}_0,\mathbf{r}) = \mathbf{L}^T(\mathbf{r}_0)\mathbf{L}(\mathbf{r})$ is the leadfield correlation between points $\mathbf{r}_0$ and $\mathbf{r}$.

Fig. 3 shows a comparison of the power computed using the classical Eq. (7) (marked with plus symbols) and by using Eq. (12) (solid red line). The source was placed at (0,0,0.084; coordinates in *m*) pointing in *x* direction. A measurement with 10,000 samples was simulated. The source was activated with white noise bandpass-filtered between 11 and 13 Hz. White noise was added to the signal resulting in a SNR of 10, 20, or 30 dB, respectively (based on the ratio of the largest singular values of signal and noise). As expected from the equations, both approaches yield identical results in this situation.

The remaining problem is the computation of the FWHM. It can be easily obtained by recognizing that the PSF of a source has a Lorentzian profile as we will show in the following derivation.

We start from the fact that the leadfield correlation R_L in Eq (12) is 1 for $\mathbf{r}_0 = \mathbf{r}$ and decreases slowly with increasing distance between the points $\mathbf{r}_0$ and $\mathbf{r}$. The smooth decrease can be approximated by a polynomial series expansion using only the first two nonzero terms

$$R_L = 1 - \left(\frac{\mathbf{r} - \mathbf{r}_0}{a}\right)^2. \tag{13}$$

a quantifies the decrease of the leadfield correlation. Now we use this approximation in Eq. (12) which results in

$$P = \frac{\mathbf{S}_{1,1}}{\left(\frac{\mathbf{r} - \mathbf{r}_0}{a}\right)^2\left(\frac{\mathbf{S}_{1,1}}{\mathbf{S}_{2,2}} - 1\right) + 1}. \tag{14}$$

Equation (14) can already be identified as a Lorentzian profile with amplitude *A* and FWHM *w* as

$$A = S_{1,1} \text{ and } w^2 = \frac{a^2}{4\left(\frac{S_{1,1}}{S_{2,2}} - 1\right)}. \tag{15}$$

Simulations

Simulations have been carried out to evaluate the validity of the approximation in Eq (13). To this end, activations were simulated at 10,000 random locations in the entire brain. A tangential orientation with respect to a spherical volume conductor model was assigned to the source. A line in *y* direction passing through the source was constructed. (The orientation of the line did not significantly change the main results presented here.) The PSF of the source was computed along this line with a spatial resolution of 0.15 mm. The simulations were carried out with a SNR of 10, 20, and 30 dB and using 32, 62, and all 122 channels of the Neuromag-122 system. All the simulations were computed twice. First, with a single source and, second, with five additional sources that were randomly placed in the brain.

Table 1
Summary of the results of the simulations

SNR	Without additional sources			With five additional sources		
	32	62	122	32	62	122
10	28.8/10.8	25.4/8.0	21.1/5.4	33.5/14.6	33.0/11.8	30.6/8.5
20	11.1/3.4	8.0/2.4	6.6/1.7	11.4/5.3	10.6/9.8	10.0/3.3
30	3.4/2.6	2.5/2.4	2.1/2.8	3.7/3.2	3.4/10.5	3.2/2.8

Note. All combinations of SNR (10, 20, 30) and number of sensors (32, 62, 122) were computed and are presented in the table. The left part of the table is based on simulations with a single source. The right part of the table describes results from simulations where five additional sources were randomly placed inside the brain. Each field contains two numbers. The first is the mean FWHM (in mm) computed from the PSF. The second number is the mean relative error (in percent) ($100*(FWHM_1 - FWHM_2)/(FWHM_2)$) of the FWHM computed from the approximation ($FWHM_1$) and directly from the PSF ($FWHM_2$).

The five interfering sources were simulated with the same activation strength as the target source. The FWHM was computed using the approximation in Eq (13) and directly from the computed PSF. All computations were initially performed using a realistic head model (BEM). The line used to compute the PSF often extended outside the brain for cortical areas which leads to distorted results especially when using the BEM. To minimize this effect, a spherical head model was used for cortical areas. This problem demonstrates the advantage of using the local approximation, especially under conditions where it is difficult to obtain a meaningful PSF.

The results of the simulations are summarized in Table 1. The rows correspond to different SNRs and the columns correspond to different numbers of sensors used for the simulation. The left part of the table is based on simulations with a single source. The right part of the table describes results from simulations with five interfering sources. Each field summarizes the results in the following format: mean FWHM (in mm) computed from the PSF/mean relative error of the FWHM in percent. It is evident that both an increase in the SNR and the number of channels reduce the FWHM and the relative error of the FWHM estimation. The increase of the relative error at 30 dB and 122 sensors is due to the discrete spatial sampling (with 0.15 mm resolution). Because the FHWM is smallest under these conditions, the relative error is dominated by errors introduced by the spatial sampling.

Mapping the spatial resolution of DICS

We now use this approximation to estimate the FWHM of the DICS filter at any given point in the brain under the assumption that there is a point source with a given SNR. This is done by computing the leadfield correlation of any voxel to the neighboring voxel. This allows the use of Eq (15) to compute FWHM *w*. In Fig. 4A, the mapping of FWHM in millimeters on anatomical MRI slices is shown.

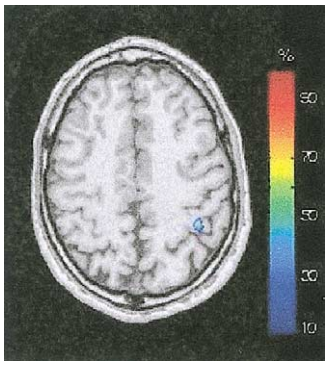

Fig. 5. Probability map of source localization. The distribution of the localization of right sensorimotor source from Fig. 4C has been obtained with the bootstrap method. The 7–13 Hz component of the mu-rhythm was localized 10,000 times. The distribution of the peak location was normalized to represent the probability that the local maximum occurs in a certain voxel. The probability map was thresholded at the 10% level.

Equation (15) was used with 20 dB SNR. The axial slices show that the FWHM of the PSF increases for subcortical areas. The slices describe the properties of the functional map independent of the data. This information is useful for assessing the performance of the spatial filter for a given measurement configuration (a given position of the head relative to a specific sensor array).

Once the measurement is performed, the FWHM of the PSF can be computed with Eq (15) using an estimate of the SNR for each voxel in the brain. This estimate is obtained from Eq (7) and is demonstrated in Fig. 4B. Five min of recording were obtained from a subject who was resting with his eyes open. The generators of spontaneous activity were localized in the 7–13 Hz frequency range corresponding to the alpha-rhythm and the low-frequency component of the mu rhythm. The tomographic power map was used for the estimation of the FWHM of the PSF. The power maxima in bilateral sensorimotor areas (more pronounced on the right side) and occipital areas (Fig. 4B) lead to a reduction of the FWHM (Fig. 4C), indicating the enhanced resolution of the spatial filter for these areas.

Confidence volumes for maxima in functional maps created with spatial filter

In the previous section, we have derived an expression which allows the computation of the FWHM of the PSF of a neural generator at a given point. This measure quantifies the data-dependent spatial resolution of the functional maps. A second essential measure which complements the FWHM is the confidence volume for the location of a local maximum in the functional map. The 95% confidence volume contains the true source location with 95% probability. This measure quantifies the uncertainty of the localization and is an important parameter for the process of assigning a local maximum to an anatomic area and for evaluating differences in localization.

We suggest the use of bootstrapping (Efron, 1979; Zoubir and Boashash, 1998) for the computation of a confidence volume. The bootstrap method does not require assumptions on the distribution of the data for which a confidence volume is needed.

The computation is performed in the following way. The raw data is split into N nonoverlapping segments which have a length appropriate for a subsequent fast fourier transform (FFT) (e.g., 1024 samples). The cross spectral density $\mathbf{C}_i$ of all channel combinations is computed separately for each segment i. N matrices are randomly drawn from this whole population (with replacement), averaged, and used in the localization procedure [e.g., Eq (7) for a power map]. The random drawing and subsequent localization is repeated a large number of times resulting in a distribution of local maxima. This distribution can be directly presented as a probability map (Fig. 5) or it can be used for the estimation of a confidence volume. In the latter case, a sphere around the most likely source location can be constructed that contains 95% (or 99%) of the local maxima. The radius of the sphere is a measure for the uncertainty of localization. It should be noted that more complex confidence volumes may be used. If the source has a preferred orientation (as is often the case), we can distinguish mainly two independent orientations (parallel and perpendicular to the source orientation). The resulting confidence volume has an ellipsoidal form represented by two independent radii.

The suggested procedure is demonstrated for the data used in Fig. 4C. The 300 segments of data were subjected to the bootstrap analysis resulting in a probability distribution of the source in the right sensorimotor cortex (Fig. 5). A grid size of 1 mm was used and the random drawing was repeated 10,000 times. In addition, the effect of the recording time was investigated. The probability map was computed for 30, 60, 120, 180, and 300 randomly drawn segments corresponding to 30, 60, 120, 180, and 300 s of recorded data, respectively.

Table 2 shows the radius of the 95% and the 99% confidence sphere in millimeters. Extending the recording time leads to a marked reduction of the radius of the confidence sphere.

Table 2
Summary of the results of the bootstrap procedure

Length (s)	95% (mm)	99% (mm)
30	8.5	11.9
60	3.5	4.9
120	1.8	2.3
180	1.5	2.1
300	1.5	1.5

Note. For different length of recording time, the radius of the 95% and the 99% confidence sphere is listed in mm. The confidence sphere is defined as the sphere containing 95% (or 99%) of the local maxima. Extending the recording time leads to a marked reduction of the radius of the confidence sphere.

Discussion

We present two measures for the characterization of functional tomographic maps obtained by spatial filtering: first, the FWHM of the point spread function (PSF) and, second, a confidence volume for the location of local maxima. The FWHM has been used before to quantify the resolution of functional maps (de Peralta-Menendez et al., 1997; Babiloni et al., 2001; Liu et al., 2002; Lutkenhoner and de Peralta-Menendez, 1997; Dale et al., 2000). In these studies, the FWHM was computed numerically from simulated data in the following way: A dipole was placed at a certain location. The dipole strength was chosen to obtain a specific SNR. The forward problem was solved and the given algorithm was applied to the simulated data resulting in a distributed representation of the pointlike source. The distance from the peak at which the peak strength was reduced by 50% was used as FWHM.

In contrast, we derived an analytic expression for the FWHM. This expression directly shows that the FWHM depends on the SNR and the leadfield correlation and allows a considerably easier use. Specifically, power maps obtained from real data can be used to estimate the FWHM. The simulations demonstrate the reliability and robustness of the proposed technique.

The ability to estimate the FWHM is also important for an appropriate choice of the grid spacing. If the smallest FWHM is considerably smaller than the grid spacing, it is more likely that a sharp representation of a source might not be detected if it happens to be located between two grid points. One could imagine a nonisotropic map where the grid spacing is adapted to the local FWHM. For a fast scanning, the grid spacing could be set to a large value (e.g., 8 mm) and the FWHM may be enhanced by increasing the regularization α trading this with a resolution reduction.

The computation of a confidence volume is of crucial relevance for the assessment and interpretation of tomographic maps. It is necessary for a reliable and objective assignment of local maxima to anatomic areas and indispensable for the identification of differences in localization between different experimental conditions. Two localizations may be regarded as significantly different if their 95% confidence volumes do not overlap.

The suggested bootstrap method is well established and is used in numerously different areas (including signal processing (Zoubir and Boashash, 1998)) for statistical assessment of data with unknown distributions.

It should be noted that the bootstrap method cannot quantify the “correctness” of the localization but only the uncertainty of the localization (using a specific algorithm) given the variability in the raw data. In addition, the computation of the confidence volume is time consuming because the localization procedure has to be performed many times. Furthermore, the grid size has to be adjusted in order to resolve differences in the location of the local maximum.

In conclusion, we present methods for assessing properties of functional tomographic maps obtained with spatial filtering techniques like DICS. These methodological advances represent a new step toward a unified framework for the statistical evaluation of MEG/EEG tomographic maps.

Acknowledgments

This study was supported by the Volkswagen-Stiftung (I/73240) and the Academy of Finland (49900). The authors thank Mrs. E. Rädisch for technical help with the MRI scans.

References

Ahonen, A., Hämälainen, M., Kajola, M., Knuutila, J., Laine, P., Lounasmaa, O., Parkkonen, L., Simola, J., Tesche, C., 1993. 122-channel SQUID instrument for investigating the magnetic signals from the human brain. Phy. Scripta T49, 198–205.

Babiloni, F., Carducci, F., Cincotti, F., del Gratta, C., Pizzella, V., Romani, G., Rossini, P., Tecchio, F., Babiloni, C., 2001. Linear inverse source estimate of combined eeg and meg data related to voluntary movements. Hum. Brain Mapp. 14, 197–209.

Brovelli, A., Battaglini, P., Naranjo, J., Budai, R., 2002. Medium-range oscillatory network and the 20-hz sensorimotor induced potential. Neuroimage 16 (1), 130–141.

Dale, A., Liu, A., Fischl, B., Buckner, R., Belliveau, J., Lewine, J., Halgren, E., 2000. Dynamic statistical parametric mapping: combining fmri and meg for high-resolution imaging of cortical activity. Neuron 1 (26), 55–67.

de Peralta-Menendez, R.G., Hauk, O., Gonzalez-Andino, S., Vogt, H., Michel, C., 1997. Linear inverse solutions with optimal resolution kernels applied to electromagnetic tomography. Hum. Brain Mapp. 5, 454–467.

Efron, B., 1979. Bootstrap methods: another look at the jackknife. Ann. Statistics 7, 1–26.

Gross, J., Kujala, J., Hämäläinen, M., Timmermann, L., Schnitzler, A., Salmelin, R., 2001. Dynamic imaging of coherent sources: studying neural interactions in the human brain. Proc. Natl. Acad. Sci. USA 98 (2), 694–699.

Gross, J., Timmermann, L., Kujala, J., Dirks, M., Schmitz, F., Salmelin, R., Schnitzler, A., 2002. The neural basis of intermittent motor control in man. Proc. Natl. Acad. Sci. USA 99 (4), 2299–2302.

Jensen, O., Vanni, S., 2002. A new method to identify multiple sources of oscillatory activity from magnetoencephalographic data. Neuroimage 15 (3), 568–574.

Lachaux, J., Rodriguez, E., Martinerie, J., Varela, F., 1999. Measuring phase synchrony in brain signals. Hum. Brain Mapp. 8 (4), 194–208.

Liu, A., Dale, A., Belliveau, J., 2002. Monte Carlo simulation studies of EEG and MEG localization accuracy. Hum. Brain Mapp. 16, 47–62.

Lutkenhoner, B., de Peralta-Menendez, G., 1997. The resolution-field concept. Electroencephalogr. Clin. Neurophysiol. 102 (4), 326–334.

Robinson, S., Vrba, J., 1997. Functional neuroimaging by synthetic aperture magnetometry (SAM), in: Yoshimoto, T., Kotani, M., Kuriki, S., Karibe, H., Nakasato, B. (Eds.), Recent Advances in Biomagnetism, Tohoku University Press, Sendai, Japan, pp. 302–305.

Rodriguez, E., George, N., Lachaux, J., Martinerie, J., Renault, B., Varela, F., 1999. Perception’s shadow: long-distance synchronization of human brain activity. Nature 397 (6718), 430–433.

Rosenblum, M., Kurths, J., 1998. Analysing synchronization phenomena from bivariate data by means of the hilbert transformat, in: Kantz, H., Kurths, J., Mayer-Kress, G. (Eds.), Nonlinear Analysis of Physiological Data, Springer, Berlin, pp. 91–99.

Rosenblum, M., Pikovsky, A., 2001. Detecting direction of coupling in interacting oscillators. Phy. Rev. E 64 (045202), 1–4.

Sekihara, K., Scholz, B., 1996. Generalized Wiener estimation of three-dimensional current distribution from biomagnetic measurements. IEEE Trans. Biomed. Eng. 43 (3), 281–291.

Singh, K., Barnes, G., Hillebrand, A., Forde, E., Williams, A., 2002. Task-related changes in cortical synchronization are spatially coincident with the hemodynamic response. Neuroimage 16 (1), 103–114.

Taniguchi, M., Kato, A., Fujita, N., Hirata, M., Tanaka, H., H. Ninomiya, T.K., Hirabuki, N., Nakamura, H., Robinson, S., Cheyne, D., Yoshimine, T., 2000. Movement-related desynchronization of the cerebral cortex studied with spatially filtered magnetoencephalography. Neuroimage 12 (3), 298–306.

Tass, P., Rosenblum, M., Weule, J., Kurths, J., Pikovsky, A., Volkmann, J., Schnitzler, A., Freund, H.-J., 1998. Detection of n: application to magnetoencephalography. Phys. Rev. Lett. 81 (15), 3291–3294.

van Veen, B., van Drongelen, W., Yuchtman, M., Suzuki, A., 1997. Localization of brain electrical activity via linearly constrained minimum variance spatial filtering. IEEE Trans. Biomed. Eng. 44 (9), 867–880.

Varela, F., Lachaux, J., Rodriguez, E., Martinerie, J., 2001. The brainweb: phase synchronization and large-scale integration. Nat. Rev. Neurosci. 4, 229–239.

Zoubir, A., Boashash, B., 1998. The bootstrap and its application in signal processing. IEEE Signal Proc. Mag. 56–76.